

Polymer-inorganic hybrid colloids for ultraviolet-assisted direct ink write of polymer nanocomposites

Philip J. Scott^a, Daniel A. Rau^b, Jianheng Wen^a, Mai Nguyen^a, Christopher R. Kasprzak^a, Christopher B. Williams^b, Timothy E. Long^{a,*}

^a Department of Chemistry, Macromolecules Innovation Institute, Virginia Tech, Blacksburg, VA 24061, United States

^b Department of Mechanical Engineering, Macromolecules Innovation Institute, Virginia Tech, Blacksburg, VA 24061, United States

ARTICLE INFO

Keywords:

UV-assisted direct ink write (UV-DIW) additive manufacturing
3D printing
Polymer nanocomposite elastomer
Hybrid latex
Silica nanoparticles
Styrene-butadiene rubber (SBR)

ABSTRACT

Inorganic-polymer hybrid colloids present a modular and tunable route to fabricate polymer nanocomposites from low viscosity precursors; however, their use in additive manufacturing remains limited. This manuscript describes photocurable “hybrid colloids” to enable layered fabrication of elastomeric nanocomposites, i.e., combination of continuous-phase photocrosslinking chemistry with hybrid colloids of water-dispersible silica nanoparticles and styrene-butadiene rubber (SBR) latex particles. Varying the relative concentrations of polymeric and inorganic particles afforded precise tuning of filler loading in the final nanocomposite and introduced a bimodal particle size distribution with desirable rheological behavior for extrusion-based additive manufacturing. Specifically, ultraviolet-assisted direct ink write (UV-DIW) processing of the photocurable hybrid colloid pastes generated free-standing green bodies, which contained a combination of SBR and silica nanoparticles. Subsequent drying of the green bodies allowed SBR particle coalescence and penetration through the scaffold and surrounding the silica nanoparticles, which yielded a semi-interpenetrating network (sIPN) nanocomposite. Facile tuning of silica concentrations in the hybrid colloid enabled tuning of both the colloidal ink rheology and mechanical properties of the final sIPN nanocomposites to achieve additive manufacturing of silica-SBR nanocomposites with ultimate tensile strains exceeding 300 % and ultimate tensile strengths above 10 MPa.

1. Introduction

Polymer nanocomposites remain a vast and rapidly evolving field, which employs a diverse toolbox of nanofillers and polymer compositions. Earlier investigations have demonstrated the synergistic capability of nanofillers to enhance many physical properties of polymeric materials, particularly at low concentrations [1]. Commonly investigated nanofillers include carbon-based (carbon nanotubes [2], graphene [3] and graphene oxide [4], carbon nanofibers [5]), metals [6] (gold [7–9], silver [10–12], copper [13,14], titanium [15], iron [16,17], aluminum [18]), ceramics and metal oxides (silica [19–24], clay [25–27], zinc oxide [28], zirconia [29], hydroxyapatite [30], cerium oxide [31,32]), and bio-based nanofillers such as cellulose nanocrystals [33,34] and biopolymer (chitin [35], cellulose [36]) nanofibers. These materials enable multiple technologies and provide enhanced performance in reinforced thermoplastics and elastomers [1,37], conductive and electroactive materials [7,38,39], dielectrics and capacitors [6,40], optical materials [41], and bioactive/biosourced

materials [11,13,42]. In particular, nanosilica has garnered significant attention due to its high reinforcing capability, low cost, low toxicity, and facile surface functionalization with well-established silane reagents. Silica composites are essential in the elastomer industry, particularly for automotive tire applications [43,44] (natural rubber, styrene-butadiene rubber, etc.) and silicones [45].

Polymer-inorganic hybrid colloids (also termed hybrid, or composite, latexes) contain both polymeric and inorganic materials in the dispersed phase and serve as a precursor to synthesizing polymer nanocomposites [46]. Their colloidal morphology offers a low viscosity medium for high molecular weight polymers, due to the lack of chain entanglements between particles, and ensures dispersion of inorganic fillers within the polymer at sub-micron length scales. Synthetic strategies for hybrid latexes often rely on miniemulsion techniques, which encapsulate inorganic nanoparticles into monomer droplets that subsequently polymerize to yield stable composite latex particles containing both polymeric and inorganic components [31,46]. Although less common in the literature, hybrid latexes also exist with each

* Corresponding author.

E-mail address: telong@vt.edu (T.E. Long).

<https://doi.org/10.1016/j.addma.2020.101393>

Received 21 April 2020; Received in revised form 30 May 2020; Accepted 17 June 2020

Available online 24 June 2020

2214-8604/ © 2020 Elsevier B.V. All rights reserved.

component present as a discrete particle (i.e., separate polymer and inorganic particles) [44,47]. In contrast to the former approach, this strategy often requires independently water-dispersible inorganic nanoparticles for incorporation into a latex polymer colloid without disrupting the colloidal stability. However, this approach expands the material diversity for polymer colloids beyond miniemulsion products (e.g., utilizing natural rubber latex) [44] and allows for additional modularity in particle loading. Synthetic techniques for this latter family of hybrid colloids include the mixture of preformed, dispersible inorganic particles into polymer latex [44,47] (i.e., latex compounding) and *in situ* generation of inorganic particles within the latex continuous phase or at polymer particle surfaces with a sol-gel process [48]. Typical applications of hybrid latexes, similar to those for pure polymer latex, focus on 2D applications such as coatings and paints, and their utilization in creating 3D nanocomposite architectures remains largely unexplored.

Direct ink write (DIW), also known as robocasting, is a material extrusion additive manufacturing (AM) platform, which fabricates three-dimensional objects from viscous liquids and pastes by selectively extruding these “inks” in a layer-by-layer manner [49]. Compared to fused filament fabrication (FFF), another leading extrusion-based AM process, DIW is not restricted to thermally-induced flow of thermoplastics, demonstrated by multiple examples of printing non-thermoplastic materials at ambient conditions [50–52]. Literature demonstrates the promise of DIW to create complex geometries of polymeric/oligomeric melts [53,54] and solutions [55] as well as inorganic suspensions [56,57] due to its ability to process materials with a wide viscosity range and a multitude of solidification mechanisms. As an example, UV-assisted DIW (UV-DIW) uses UV irradiation to photocure extruded photopolymers that have viscosities multiple orders-of-magnitude greater than the suitable range for vat photopolymerization (VP), another major AM platform [55].

Using an applied pressure, DIW selectively extrudes inks through a nozzle onto a substrate [49]. Therefore, these inks must undergo both flow through the nozzle and rapid solidification upon deposition to retain their as-deposited shape and yield free-standing, stackable layers. Material strategies address this processing requirement by using selective liquid-solid transitions induced through (i) crosslinking (chemical or physical) [55,58,59], (ii) yield-stress rheological behavior [51,53], (iii) thermal flow and solidification [60], or (iv) solvent evaporation [61]. For case (i), reactive, shear-thinning liquid inks (e.g., polymeric solutions or oligomeric melts) readily extrude through the nozzle with subsequent solidification by crosslinking, activated with photo-irradiation [55] (e.g., photoinitiated acrylate crosslinking), heat [59], mixing with nucleophilic initiators [52,62] (e.g., 2-part epoxy systems), or physical interactions (e.g., ionic association) [58]. For case (ii), yield stress rheological behavior provides shear-induced liquid-solid transitions, which enable solid pastes to flow under applied stress and re-solidify rapidly upon exiting the nozzle. Many filled polymeric and oligomeric materials display this desirable rheological behavior, and recent examples include filled (e.g., graphene oxide, nanoclay) epoxy resins [54,63], shear-thinning hydrogels [64], particle suspensions [51,53], and colloidal gels [57,65], which enable DIW printing of functional materials that combine mechanical performance with structural complexity. Many examples combine mechanisms i & ii to aid in the generation of shape and the manifestation of mechanical properties during DIW processes [63,66,67]. However, high molecular weight polymers are not suitable for DIW as a greater amount of chain entanglements induces melt and solution viscosities above the suitable maximum for DIW (up to approximately 10^5 Pa·s with appropriate shear-thinning behavior) [54,68]. Furthermore, the inclusion of inorganic fillers to the polymer further increases viscosity leading to nozzle clogging or inability to extrude at the available pressures [69]. As a result of the viscosity constraints due to applied pressure limitations of the extruder, filled thermoplastics printed via FFF are limited to 40 wt% filler [69].

Polymer colloids mitigate the molecular weight-viscosity relationship through preventing long-range entanglement as chains are sequestered into discrete particles. Furthermore, the polymer colloids often exhibit shear thinning behavior, presenting an opportunity for polymer colloids as high molecular weight DIW inks. Colloidal gel DIW inks comprise high concentrations of particles in a liquid medium, which physically interact to form a solid colloidal gel. Above a critical stress or strain, this colloidal gel network disrupts, allowing particles to flow past each other, and the colloid rapidly transitions to liquid-like rheological behavior. Upon removal of shear stress, the structure reforms and the material solidifies [70,71]. Investigations of colloidal DIW inks include poly(ethylene imine)-coated silica nanoparticles in water [65], concentrated polymer colloids [72,73], and inorganic particles suspended in a small-molecule dispersant [57] or liquid oligomer melts [54]. Although concentrated colloids display ideal rheological behavior for DIW, utilization of inorganic-polymer hybrid colloids to simultaneously introduce high molecular weight polymers and facile incorporation of inorganic fillers for DIW remains unexplored.

Herein, we report, to the best of our knowledge, the first example of additive manufacturing of inorganic-polymer hybrid colloids. Our research groups have recently developed a novel, photoactive continuous-phase scaffolding approach to enable VP additive manufacturing of polymeric latexes as a versatile strategy to fabricate complex geometries of high molecular weight elastomers from low-viscosity precursors [74]. Replacing a fraction of polymer particles with inorganic nanoparticles allows access to high-performance nanocomposites. High particle concentrations, concomitant with the introduction of the smaller silica particles, introduce yield-stress rheological behavior and position these hybrid colloids as ideal candidates for DIW printing. The hybrid colloids were therefore equipped with two solidification mechanisms (i & ii), which include a reversible, shear-dependent solid-liquid transition that enabled both flow through the nozzle and retention of the deposited shape, and a subsequent, irreversible gelation by continuous-phase photocrosslinking to provide a robust network capable of supporting subsequent layers. Upon drying of printed objects, coalescence of latex polymer particles throughout the photocrosslinked scaffold surrounds the silica nanoparticles and yields high-performance reinforced elastomeric nanocomposites with tensile strains exceeding 300 % and tensile strengths approaching 10 MPa.

2. Materials and methods

2.1. Materials

Carboxylated styrene-butadiene rubber (SBR) latex (Rovene 4176) was generously donated by Mallard Creek Polymers Inc. The latex has a solids content of 50 wt% in water and a particle diameter range of approximately 120–170 nm. The SBR copolymer was approximately 50/50 by weight styrene and butadiene with a low level of carboxylic acid monomer neutralized with ammonia to provide colloidal stability. The SBR latex polymer contains a high insoluble (gel) content due to intra-particle crosslinking side reactions that occur during emulsion polymerization.

1-vinyl-2-pyrrolidinone (NVP), poly(ethylene glycol) 575 g/mol (PEGDA 575), lithium bromide (LiBr), (3-aminopropyl)triethoxysilane, and succinic anhydride were purchased from Millipore Sigma and used as received. Methyl ethyl ketone (MEK), dimethyl phenylphosphonite and 2,4,6-trimethylbenzoyl chloride were purchased from Alfa Aesar and used without further purification. Colloidal silica nanoparticles (10–15 nm) dispersed in MEK (MEK-ST) were generously donated by Nissan Chemical Corporation. HPLC-grade tetrahydrofuran (THF), dimethyl formamide (DMF), diethyl ether, and hexanes were purchased from Fisher Scientific and used without further purification.

2.2. Analytical methods

Dynamic light scattering (DLS) was performed with a Malvern Zetasizer Nano at 25 °C. Thermogravimetric analysis (TGA) was performed with a TA Instruments Q500 at a rate of 10 °C/min and an isothermal drying step at 120 °C for 10 min.

Tensile tests were performed with an Instron 5500R equipped with a 200 lb load cell at 50 mm/min. Tests were conducted on (i) dogbones that were both die-cut (ASTM D-638 V) from photocast and dried films, and (ii) dogbones printed via UV-assisted direct ink write (UV-DIW) (ASTM D-638 IV, scaled proportionally to a 55 mm length). Differences between the mechanical properties of tensile bars printed with x-y tool path bead orientations of 0°, 45°, and 90° with respect to the elongation direction were compared using a one-way ANOVA, where a value of $P < 0.05$ was considered statistically significant. Cyclic experiments were performed on the same Instron instrument at a rate of 200 %/min with a 30 s hold at 0% strain between cycles.

Dynamic mechanical analysis (DMA) was performed on a TA Instruments Q800 at 1 Hz, 3 °C/min, and 0.2 % strain.

Rheological analysis was performed on a TA Instruments DHR-2 rheometer with a concentric cylinder geometry (28 mm bob diameter, 42 mm bob length, 30.4 mm cup diameter) for both continuous flow and oscillatory experiments at 25 °C. An oscillatory time sweep experiment was performed to investigate the recovery time of colloidal network structure to gauge wait time between experiments. Stress and strain sweeps were performed at a constant frequency of 1 Hz.

Photorheology was performed with the same rheometer equipped with a 20 mm parallel plate geometry with a UV light guide attachment and OmniCure S2000 Spot UV Curing System light source. Photorheological tests were performed at 0.2 % strain, 1 Hz, and with a measured UV intensity of 250 mW/cm² averaged across a spectral range of 320–500 nm. Scanning electron microscopy (SEM) samples were freeze-fractured in liquid nitrogen prior to imaging on a FEI Quanta 600 FEG utilizing the back-scattering detector and 20 kV accelerating voltage. Samples were sputter-coated with 7 nm of gold/palladium for imaging.

2.3. Synthesis of lithium acylphosphinate photoinitiator (LAP)

Lithium acylphosphinate photoinitiator (LAP) was synthesized according to a previous procedure from literature [75,76]. In a typical example 3.00 g (17.5 mmol) of dimethyl phenylphosphonite was added to a 250-mL round bottomed flask and purged with argon for 15 min while stirring. 3.20 g (17.5 mmol) of 2,4,6-trimethylbenzoyl chloride was added dropwise via syringe to the flask while stirring and allowed to react 18 h. It is important to note that methyl chloride is a toxic, gaseous byproduct of this reaction and therefore the reaction purge outlet was bubbled through an aqueous ethanolamine trap. 6.1 g (70.1 mmol) of LiBr was dissolved in 100 mL of MEK and the solution was added to the reaction. The reaction was subsequently heated to 50 °C for 10 min after which a white precipitate formed. The reaction was then cooled and allowed to rest at room temperature for 4 h to allow full precipitation. The supernatant was decanted, and the white powder precipitate was washed three times with MEK. The LAP powder was then dried at room temperature *in vacuo* overnight and stored in a sealed amber jar.

2.4. Surface functionalization of silica nanoparticles

Surface functionalization of colloidal silica nanoparticles followed methods described previously in literature [77]. In a typical example, 100 g of a colloidal silica in MEK dispersion (25 g dry silica) was combined with 100 mL of THF in a sealed 500-mL round bottomed flask and purged 20 min with argon while stirring vigorously. 3.258 g (14.7 mmol) of (3-aminopropyl)triethoxysilane was added to the flask. The reaction was heated to 60 °C and allowed to react for 16 h. The reaction

dispersion was subsequently poured into a series of 50-mL centrifuge tubes, each diluted 5x with hexanes, and centrifuged at 6000 rpm for 5 min to precipitate the particles. The supernatant was discarded, and the particles were redispersed in THF. This purification process was repeated 3x before finally redispersing the amine-functionalized nanoparticles in 200 mL DMF in a 500-mL round bottomed flask and purged with argon for 20 min while stirring. 4.22 g (42.2 mmol) of succinic anhydride was dissolved in 10 mL DMF and added via syringe and the reaction was allowed to proceed for 12 h at room temperature. The resultant carboxylic acid (COOH) functional particles were precipitated from diethyl ether, centrifuged 3 × (in a similar fashion as described above), and finally stored as a dispersion in ethanol for storage. Degree of functionalization, expressed as mmol COOH / g silica, was determined via potassium hydroxide titration in ethanol.

2.5. Design of photocurable polymer-inorganic hybrid colloids

The design of all hybrid colloids targeted a constant total solids (SBR polymer and/or silica) content in water and liquid scaffold precursors (NVP & PEGDA). The composition of the solids was then systematically altered from 0% to 50 % silica (0:100 to 50:50 Silica:SBR) without altering the total solids content of the colloid. To these hybrid colloids compositions, a constant loading of scaffold precursors (NVP& PEGDA) was added (3.56:1 Solids:Scaffold, 2.5:1 NVP:PEGDA) which was experimentally determined to provide sufficient greenbody modulus (i.e., $G' > 10^4$ Pa).

In a typical example, a net solids content of 40 wt% solids in water and scaffold precursors was targeted with a solids ratio of 50:50 Silica:SBR, i.e. 20 wt% each for the SBR polymer and silica. COOH-functionalized silica nanoparticles (NP-COOH) were precipitated from stock ethanol solution by the addition of diethyl ether and centrifugation at 6000 rpm for 5 min. The supernatant was decanted, and the particles dried at room temperature in a vacuum oven to remove all solvent. 2.25 g of dried nanoparticle was dispersed in a solution of 3.16 g deionized H₂O, 0.903 g NVP, 0.361 PEGDA (575 g/mol), and 50.0 mg LAP by vortex and sonication until forming a viscous, clear dispersion with an amber hue. 4.688 g of SBR latex was added to the dispersion and the hybrid colloid was vortex until thoroughly mixed. Due to the high viscosity of high-silica hybrid colloids, the retention of bubbles proved an issue for the formation of pore-free photocured films and objects. Light centrifugation (1000 rpm, 2 min) enabled the removal of bubbles from the paste-like colloids without causing sedimentation of the particles.

2.6. Film preparation

As an illustrative example, 3 g of photocurable hybrid colloid was added to a petri dish (9 cm diameter) and irradiated for 30 s on each side with a belt-fed photocuring system (LC-6B) from Fusion UV systems Inc. equipped with a 100 W bulb. The films were subsequently dried in vacuum oven at 40 °C overnight to remove water and promote SBR particle coalescence and semi-interpenetrating network (sIPN) formation. The sIPN nanocomposite films were then solvent extracted as described in Section 2.8. Dogbones were cut from the films using an ASTM D-638-V die and used directly for tensile testing.

2.7. UV-DIW printing process

Shown in Fig. S5, the Ultraviolet-Assisted Direct Ink Write (UV-DIW) printer consisted of two Zaber A-LST500 linear slides that provided the extruder 500 mm of in the XY direction and a Zaber A-LST250 linear slide that provided the build plate 250 mm of travel in the Z direction. The printer was controlled with a custom-built LabVIEW control software that used standard GCODE to control the printer's movements and turn the extrusion on and off. A Nordson EFD Ultimius V DIW System was responsible for extruding material. A Keynote

Photonics LC4500-UV Digital Light Processing (DLP) projector provided UV-irradiation at 405 nm with a measured intensity of 14 mW/cm² on the build plate was responsible for curing the printed photosensitive ink (Fig. S5). The projector is mounted adjacent to the extruder, which allows the entire layer to be extruded and then be cured homogeneously at once following printing. This *ex-situ* curing method eliminates nozzle clogging due to unwanted photocuring of the material at the nozzle exit [50].

The hybrid latex inks had the appropriate rheological behavior to retain shape after deposition without the need for immediate UV curing. However, by exposing each layer to UV irradiation for a fixed period after deposition ensures the ink was not over cured and enough photocurable groups remained to form a strong interlayer adhesion with the next layer. Additionally, a homogenous cure of each layer contributed to more isotropic material properties, as measured in the x-y plane (Fig. 9C and D).

The 30:70 and 50:50 silica:SBR ink formulations were printed using a stainless-steel nozzle with an inner diameter of 0.61 mm and 12.7 mm length supplied by Nordson EFD. Parts were printed onto glass substrates with a deposition speed of 4 mm/s and each layer was exposed to UV irradiation for 15 s. 50:50 Silica:SBR inks were extruded at a pressure between 41.4 and 48.3 kPa. 30:70 Silica:SBR inks were extruded at a pressure between 10.3 and 17.2 kPa. Extrusion pressures varied within the listed range due to slight variability between ink batches. Due to evaporation of the continuous phase (Water and NVP), nozzle clogging was occasionally observed. Clogging was reduced by purging the nozzle between prints at high pressures (+200 kPa) for ~5 s and frequently replacing the nozzle.

Tensile bars consisted of three 200- μ m thick layers. Truss and Honeycomb structures (Fig. 9A) were printed from twenty-five 250- μ m thick layers. Extrusion toolpaths were varied from 0, 45, and 90° orientation with respect to elongation direction, in the x-y plane. Extrusion roads spacing was set to 650 μ m.

2.8. Post-cure processing

All photocured green bodies were dried at 40 °C overnight in a vacuum oven to facilitate water removal for SBR particle coalescence and semi-interpenetrating network (sIPN) formation. Parts were then extracted in 5/95 v/v THF and water with solvent exchanges at 2, 4, and 12 h. The solvent was then changed to pure THF with solvent extractions at the same intervals to remove the water. Extracted objects were then dried in a vacuum oven at room temperature overnight to remove THF.

3. Result and discussion

Fig. 1 illustrates the strategy for additive manufacturing of elastomeric nanocomposites using UV-DIW of photocurable polymer-inorganic hybrid colloids. Our previous report introduced the ability to 3D print latex polymeric colloids upon photoactivated network formation in the continuous phase, which yielded a particle-imbedded hydrogel “green body” [74]. Subsequent water removal enabled the formation of semi-interpenetrating polymer networks (sIPN) due to the coalescence of polymer nanoparticles throughout the photocrosslinked scaffold. This continuous-phase photocrosslinking strategy afforded unique modularity in particle selection and combination. Incorporation of water-dispersible inorganic nanoparticles together with polymer particles enabled a facile route to printable nanocomposites. Carboxylated silica nanoparticles contained similar negative surface charges to carboxylated styrene-butadiene (SBR) particles and readily mixed with polymer latex without disrupting colloidal stability. The addition of photocrosslinkable network precursors into the continuous phase yielded stable, photocurable hybrid colloids amenable to UV-based AM processes. Photocrosslinking and subsequent SBR coalescence throughout the scaffold containing the silica nanoparticles yielded an

elastomeric nanocomposite without disruption in the geometric fidelity of the printed part.

3.1. Photocurable hybrid colloid design

Carboxylation of colloidal silica nanoparticles using efficient silane functionalization [77] enabled dispersibility in aqueous media, as illustrated in Fig. 2. Condensation of (3-aminopropyl)triethoxysilane with surface silanol groups yielded amine-functionalized nanoparticles. Subsequent nucleophilic ring-opening of succinic anhydride with these amines generated surface-bound carboxylic acids. Titration of the surface acids confirmed a surface loading of approximately 0.350 mmol COOH/g silica, which corresponded to an approximate surface concentration of 0.84 acid-groups/nm². Upon stoichiometric addition of triethylamine, the generation of negatively charged triethylammonium carboxylates enabled colloidal stability and dispersibility in water. Dynamic light scattering (DLS) measurements (Fig. 2B) confirmed nanoscale dispersion of the silica in water with a particle size of approximately 12 nm.

All colloids in this study maintained a constant solids (SBR and silica) content of 40 wt%, and the liquid continuous phase consisted of water and the scaffold precursors n-vinyl pyrrolidone (NVP) and poly (ethylene glycol) diacrylate (PEGDA, 575 g/mol). This target solids loading allowed for a small amount of water to disperse the silica nanoparticles prior to mixing with the latex. Facile mixing and systematic variation of the solids content from pure SBR particles (0:100 silica:SBR) to equal parts by mass of silica and SBR (50:50) yielded stable, photocurable hybrid colloids with tunable inorganic filler content.

3.2. Rheological analysis of photocurable hybrid colloids

Shear thinning behavior is a well-studied phenomenon in dispersed systems, including latex colloids [78]. Typical investigations demonstrate an increase in viscosity with volume fraction of solids (ϕ_{solids}), owing to increased interactions between particles as the colloid becomes more concentrated [78]. However in this work, the density of silica (~2 g/cm³) was roughly twice that of SBR [79] (0.94 g/cm³), and therefore increasing the silica:SBR mass ratio caused a decrease in ϕ_{solids} from approximately 0.39 to 0.32, for 0:100 and 50:50 silica:SBR, respectively, despite the constant total solids mass fraction of 40 wt%. However, Fig. 3 illustrates a sharp increase in viscosity and shear thinning with silica loading which is analogous to systems with increased ϕ_{solids} .

It is important to consider the impact of the bimodal particle distribution generated by mixing the highly disparate silica (12 nm) and SBR (122 nm) particle sizes. Previous investigations into the rheology of highly bimodal colloids (containing two particle distributions with a large/small diameter ratio, $\kappa > 5$) provide insight into this observed increase in viscosity with silica nanoparticle incorporation (Fig. 3) [80–83]. Highly bimodal systems are well known to exhibit attractive osmotic depletion forces between the larger particles due to the expulsion of the smaller particles as they approach each other. These attractive forces have been shown to increase colloid viscosity and induce colloidal gelation at high concentrations [81,84–88]. For the case of this study, κ is approximately 10, and therefore this phenomenon is expected as a dominant contribution to the viscosity increase and colloidal gelation observed with increasing silica nanoparticle incorporation (Fig. 4). Furthermore, a greater number of small particles is necessary to achieve a given solids mass loading (40 wt% in this study) than large particles, and particle-particle interactions increase with particle concentration which can increase viscosity [53]. In this work, the size difference between silica nanoparticles and SBR latex particles caused the overall particle concentration to increase by a factor of approximately 400 from the pure SBR latex (0:100 silica:SBR) to the 50:50 silica:SBR hybrid colloid, while maintaining a constant solids content of

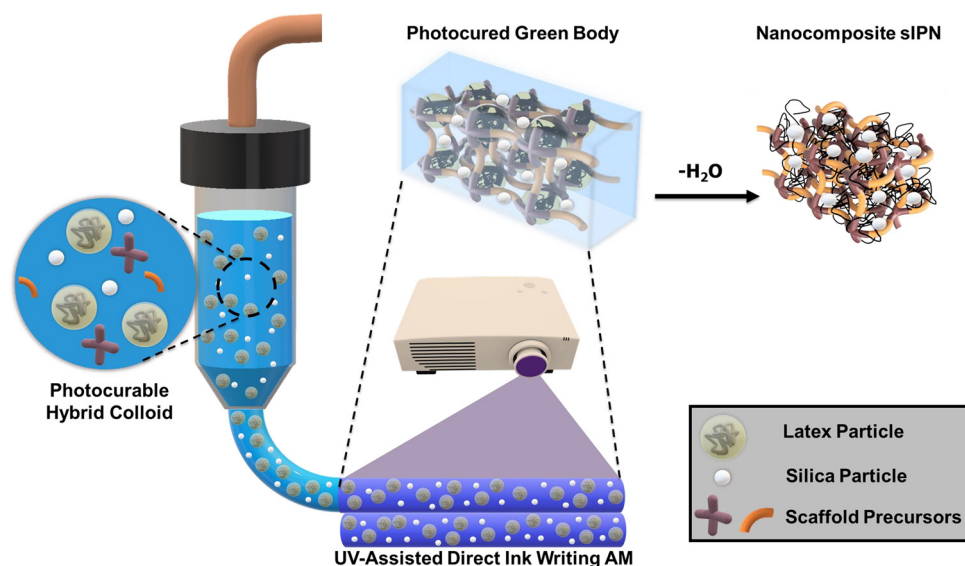


Fig. 1. Photocurable polymer-inorganic hybrid colloids enable UV-DIW additive manufacturing (AM) of hydrogel green bodies, which yield semi-interpenetrating polymer network (sIPN) nanocomposites upon removal of water.

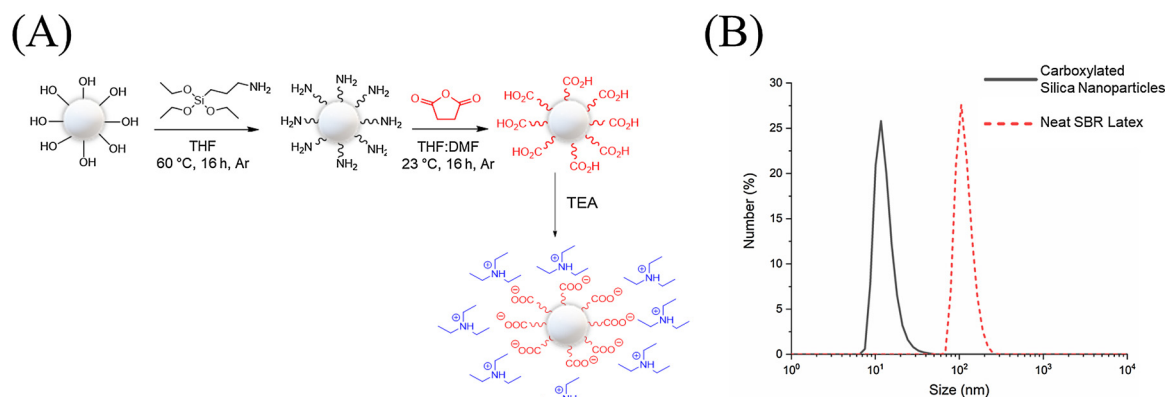


Fig. 2. (A) Carboxylate functionalization of silica nanoparticles enables water dispersibility. (B) Dynamic light scattering confirms the size of dispersed nanosilica and polymer particles in water (1 wt%).

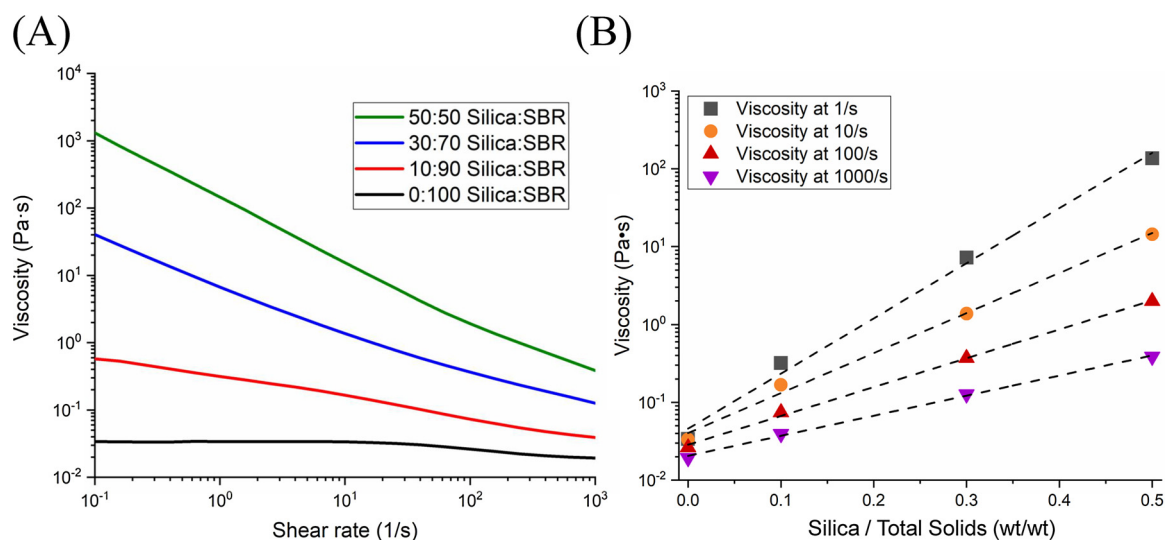


Fig. 3. (A) Steady-state shear analysis elucidates shear thinning behavior for all colloids with increasing viscosity at higher silica loadings (higher silica:SBR). Total solids content is constant between all samples (40 wt%). (B) Viscosity at various shear rates as a function of fractional silica in the total solids (silica:SBR), ie. 30:70 silica:SBR corresponds to 0.3.

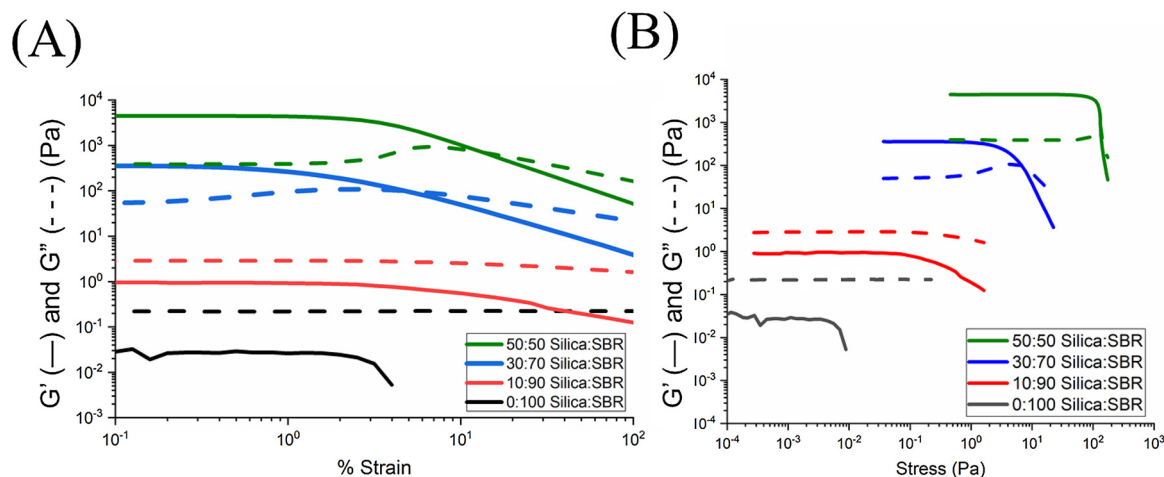


Fig. 4. Oscillatory rheology experiments elucidate shear-dependent crossovers of storage G' (—) and loss G'' (---) shear moduli for high-silica hybrid colloids. (A) Strain sweep and (B) stress sweep experiments elucidate critical yield strains and stress, respectively.

40 wt%. Increased particle concentration facilitates physical particle-particle interactions and has been shown to enable the formation of stronger colloidal gels [53], which agrees with our observations. Although the full scope of interactions in these complex colloidal systems requires further investigation, these established colloidal interactions provide insight into the observed increase in viscosity and occurrence of colloidal gelation behavior with increasing silica:SBR (Fig. 3 & 4).

VP is generally limited to printing resins with a maximum viscosity of 10–15 Pa·s [89,90], thus prohibiting VP printing of a silica:SBR ratio above 10:90 (Fig. 3). DIW successfully prints higher viscosity liquids that are unsuitable for VP and therefore provides an avenue for 3D printing of the high-silica hybrid colloid pastes. During DIW extrusion, the nozzle applies shear rates of $\sim 50 \text{ s}^{-1}$, reducing the viscosity of the 30:70 in. to 0.5–0.6 Pa·s and the 50:50 in. to 3–4 Pa·s due to the observed shear-thinning behavior.

In addition to shear-thinning behavior, the occurrence of rheological solid-liquid transitions positions the high-silica hybrid colloids as uniquely ideal candidates for DIW printing. Oscillatory rheological measurements probed the storage (G') and loss (G'') shear moduli of each colloidal ink over increasing shear strains and stress (Fig. 4). Generally, values of $G' > G''$ indicate “solid-like” properties, which is an ideal state for DIW ink to exhibit minimal flow and deformation upon deposition. Conversely, $G'' > G'$ values indicate “liquid-like” behavior and flow, which is ideal for extrusion through the nozzle [51].

As discussed previously, many DIW examples utilize the yield-stress behavior to induce flow under a shear stress from extrusion through the nozzle and to achieve subsequent solidification upon deposition; when shear stress is removed, the material retains the as-deposited shape [51,53,54,57,65,72,73]. Hybrid colloids with a bimodal distribution enabled tuning of this phenomenon through relative particle concentrations, as shown in Fig. 4. At 30:70 silica:SBR and above, the colloids exhibited ideal yield stress rheological behavior for DIW. These colloids were solid-like ($G' > G''$) at low shear strain and stress; however, beyond a critical yield point, the colloidal structure rapidly disrupted, and the colloid underwent a modulus crossover to the liquid-like state. Upon removal of this stress, the colloids rapidly re-solidified. Silica:SBR mass ratios below 30:70 did not exhibit a shear yield stress, and these inks behaved entirely as low-viscosity liquids ($G'' > G'$) at all measured shear strains/stresses. This precluded their use in DIW printing due to their tendency to flow and spread upon deposition, which made high resolution features and subsequent layers impossible to achieve. Shear moduli systematically increased with silica content (particle concentration), and the 30:70 and 50:50 silica:SBR ratios provided critical yield stress/strain values that followed a similar trend. In sharp contrast to traditional filled inks, which increase vol % filler to

achieve yield stress behavior [53], these hybrid colloids decreased in vol % solids with increasing silica:SBR (at constant wt% solids). However, as discussed previously, the increase in *particle* concentration with the addition of the smaller silica nanoparticles significantly increased the number of charged surfaces and decreased the average distance between particles. This facilitated greater particle-particle interactions, which yielded stronger colloidal networks, as evidenced with greater shear moduli and higher yield stresses, as observed in Fig. 4. It is important to note that because the rheological behavior was primarily determined by net particle concentration and the bimodal particle distribution (as discussed previously), tuning of the latter parameter will enable further adjustment of rheological behavior for either VP for DIW regardless of desired silica content (e.g., high-silica liquids for VP or low silica pastes for DIW), with the use of larger silica particles or smaller SBR particles.

It is important to compare this yield-stress behavior to stresses applied by the DIW process to evaluate their relevance for AM. Eq. (1) describes the calculation of maximum shear stress (τ) imparted by the DIW nozzle during extrusion [63].

$$\tau = \frac{\Delta P}{2L}r \quad (1)$$

In this study, a nozzle length (L) of 12.7 mm and radius (r) of 0.305 mm was maintained. The 30:70 silica:SBR was extruded at an experimentally determined applied pressure (ΔP) of 13.79 kPa, corresponding to a maximum shear stress of 165.6 Pa (estimated from Eq. 1), well above its measured shear modulus crossover stress of 7.5 Pa. Similarly, the 50:50 Silica:SBR was extruded at 44.82 kPa, corresponding to a maximum shear stress of 538.1 Pa, well above its shear modulus crossover stress of 129 Pa.

The timescale of the recovery of colloidal structure to its solid-like state after the removal of shear stress is critically important for ensuring shape retention upon deposition. To measure the time of structure yield and recovery, Fig. 5 illustrates an oscillatory shear experiment that alternates between low (0.1 %) and high (50 %) strains that are below and above the yield point of both the 30:70 and 50:50 silica:SBR hybrid colloid compositions (Fig. 4). The step change from high to low strain mimics the removal of stress when the material is extruded from the nozzle, and thus elucidates how rapidly the network structure reforms to exhibit solid-like ($G' > G''$ crossover) behavior.

Both higher-silica hybrid colloids (30:70 and 50:50 silica:SBR) exhibited rapid transitions between flow and solidification at high and low strains, respectively, and consistent reproducibility of this transition was observed over multiple cycles. The G'/G'' crossovers occurred nearly instantaneously, suggesting that the inks would transition to

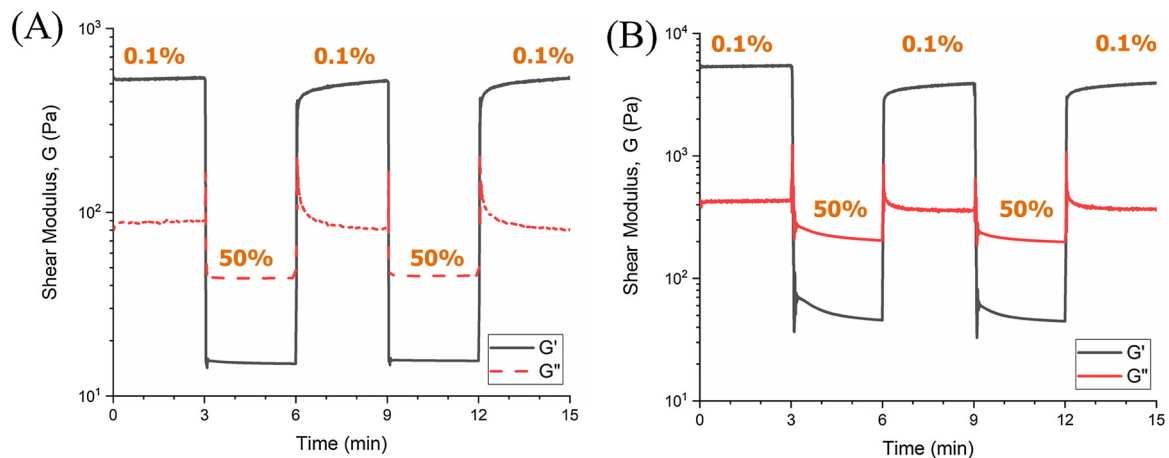


Fig. 5. Hybrid colloids at (A) 30:70 silica:SBR and (B) 50:50 silica:SBR exhibit rapid and reversible crossovers at low (0.1 %) and high (50 %) strain amplitudes. Reversible liquid-solid transitions evident by crossovers of shear storage (—) and loss (---) modulus.

solid-like behavior soon after exciting the DIW nozzle and the extruded bead would exhibit minimal spreading. After crossover to solid-like properties, the recovery of storage modulus progressed over the course of minutes and approached the original modulus exhibited before disruption within 3 min for 30:70 silica:SBR (Fig. 5A). The 50:50 silica:SBR colloid displayed a near-instantaneous crossover; however, the recovery of the G' modulus was slower than that of the 30:70 in. and did not fully recover to the original value over the observed 3 min interval (Fig. 5B). This is likely explained by the significantly higher storage modulus of the 50:50 colloid (approximately an order-of-magnitude), which restricts mobility and slows the recreation of colloidal network structure.

3.3. Evaluation of photocuring behavior of hybrid colloids

Although often utilized in lieu of yield-stress behavior [55], photocrosslinking provided a second, irreversible solidification mechanism for the hybrid colloids and thus established a multi-modal processing window for UV-assisted DIW. While the reversible yield-stress behavior enabled extrusion and subsequent retention of the as-deposited shape, photocrosslinking increased the strength of the deposited material to support the weight of subsequently deposited layers. In addition, the increased strength enabled handling of the green body and minimized warping during removal from the printer for drying.

Fig. 6 illustrates the photoactivated crosslinking chemistry, which produced a scaffold network in the continuous phase that surrounded the particles and permanently solidified the colloid. This green body comprised a water-swollen hydrogel embedded with both SBR and silica particles. Fig. 6B details photorheological measurements across all investigated silica:SBR mass ratios. These measurements occurred at low oscillatory strains (0.2 %), and therefore the higher-silica colloids displayed solid-like behavior prior to the onset of UV irradiation (250 mW/cm²) at the 30-second mark. Upon irradiation, G' and G'' for all colloids rapidly increased, and liquid colloids (below 30:70 silica:SBR) achieved permanent crossovers within 5 s. Photorheology measurements irradiated each sample through a 500- μ m gap between the parallel plates, which was larger than the target UV-DIW layers of 250- μ m, confirming the capability to achieve adequate curing depths at low exposure times (< 10 s) despite light scattering effects by the particles.

As observed in our previous investigations [74], drying of green bodies *in vacuo* enabled the SBR particles to coalesce throughout the photocrosslinked scaffold, yielding a semi-interpenetrating network (sIPN). The loss of discrete mesoscale SBR phases decreased the scattering of visible light and, as a result, the networks became translucent. Fig. 6C demonstrates this same observation for the unfilled sample; however, the silica-loaded sIPN's exhibited increasing opacity with

silica concentration. Because the individual particles were too small to scatter visible light, as evidenced by their formation of clear dispersions in water, this opacity suggested silica aggregation to length scales greater than the wavelength of visible light.

Designing hybrid colloids on a particle-by-particle basis, in contrast to composite or encapsulated particles from miniemulsion, enables precise tuning of composition and final filler content. Thermogravimetric analysis (Fig. S2) confirmed silica loading from 0 to 46 wt% (for 0:100 and 50:50, respectively) in the final sIPN nanocomposite, which was tuned through facile mixing of pure SBR and aqueous silica dispersions. Hybrid colloids comprised 40 wt% solids (silica and SBR), approximately 10 wt% liquid scaffold precursors (NVP, PEGDA), and 50 wt% water. After water removal, the final sIPN comprised approximately 80 wt% silica/SBR and 20 wt% photocrosslinked scaffold network. The latter remained constant across all colloid compositions and provided sufficient green body modulus for printing ($\sim 10^4$ – 10^5 Pa).

3.4. Microscopic and (Thermo)mechanical analysis of sIPN nanocomposites

Scanning electron microscopy (SEM) of freeze-fractured film surfaces offered insight into the size and distribution of silica particles throughout the sIPN. Fig. 7 depicts SEM micrographs for loadings from the unfilled (0:100 silica:SBR) to the highest filled (50:50 silica:SBR) compositions. Imaging of backscattered electrons enabled visible contrast between silica aggregates and the polymer matrix. Energy dispersive X-ray spectroscopy (EDS) (Figs. S3 and S4) provided elemental analysis to confirm the chemical identity of imaged structures based on relative concentrations of carbon, oxygen, and silicon. As discussed previously, opacity increased with silica loading, which suggested aggregation beyond the 12 nm diameter of individually dispersed silica nanoparticles. Silica aggregates clearly appeared for all filled systems, with a trend toward larger sizes for higher silica concentrations. SEM confirmed the presence of uniquely large aggregates at 50:50 silica:SBR. However, 10:90 and 30:70 Silica:SBR exhibited evenly distributed microscale dispersions of silica throughout the film. It is important to note that only larger silica aggregates are visible with these SEM experiments, and therefore, these micrographs do not preclude the presence of individually dispersed silica nanoparticles. Since DLS does not provide evidence of micron-scale particles, silica aggregation likely occurred during either the photocuring or drying/coalescence stages. The latter is a more plausible explanation as coalescence and penetration likely provided sufficient force to drive aggregation of previously dispersed silica nanoparticles. Capillary forces during drying may also provide silica aggregation at higher particle loadings. However, this

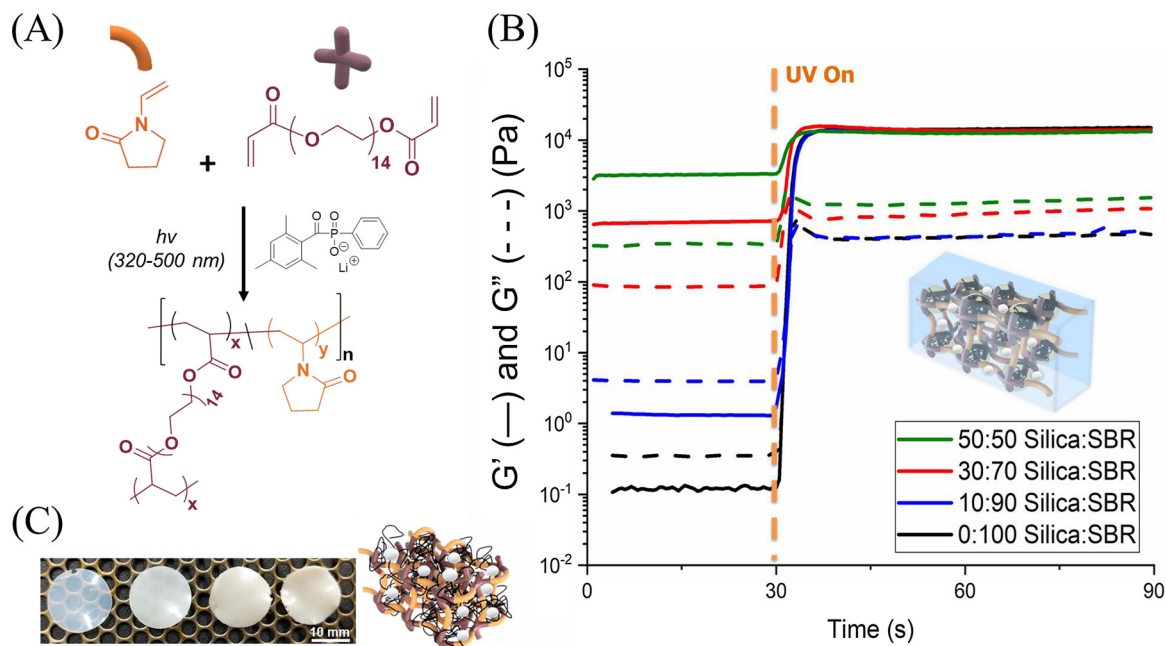


Fig. 6. (A) NVP and PEGDA provide photocrosslinkable scaffold precursors in the continuous phase of colloids. (B) Photorheology elucidates rapid photocuring at both low and high silica contents. Irreversible solidification evident by increase of shear storage (—) and loss (---) moduli, with crossovers evident for liquid 10:90 and 0:100 silica:SBR samples. Inset shows graphical representation of photocured green body (C) Dried nanocomposite IPN films with 0:100, 10:90, 30:70, and 50:50 silica:SBR, from left to right and a graphical representation of sIPN nanocomposite.

mechanism of sIPN formation from latex is unprecedented beyond our own investigations, and future studies are necessary to better understand this phenomenon.

In this case, the allure of inorganic nanofillers arose from their potential to strongly direct and reinforce the (thermo)mechanical properties of elastomers. Combining the modular tunability and processing advantages of hybrid colloids with the functional effects of

nanofillers introduced the potential to process high-performance and functional materials at low temperatures and forces with the geometric complexity characteristic of additive manufacturing. Dynamic mechanical analysis (DMA) probed the thermomechanical effects of nanosilica incorporation in the sIPN nanocomposites (Fig. 8A). Targeting various silica concentrations enabled tuning of the reinforcement of the rubbery plateau tensile modulus (E') by over three orders-of-magnitude.

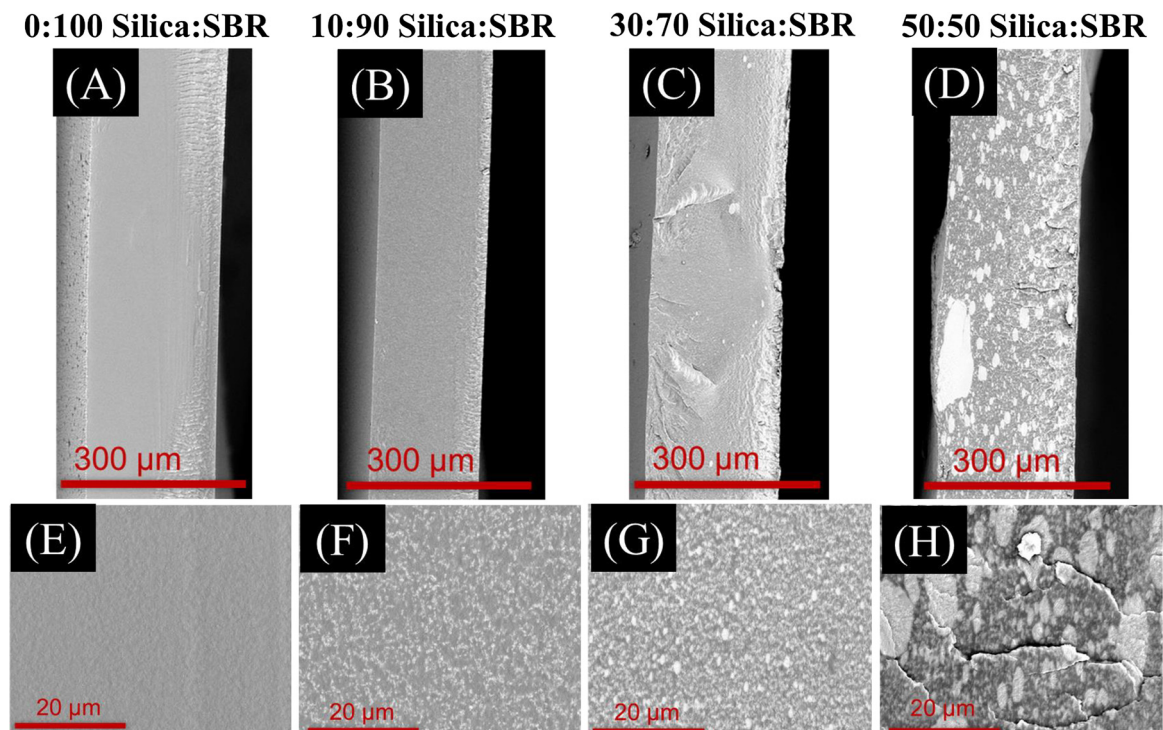


Fig. 7. SEM analysis of freeze-fractured surfaces of IPN nanocomposites at compositions: (A&E) 0:100 Silica:SBR, (B&F) 10:90 Silica:SBR, (C&G) 30:70 Silica:SBR, and (D&H) 50:50 Silica:SBR.

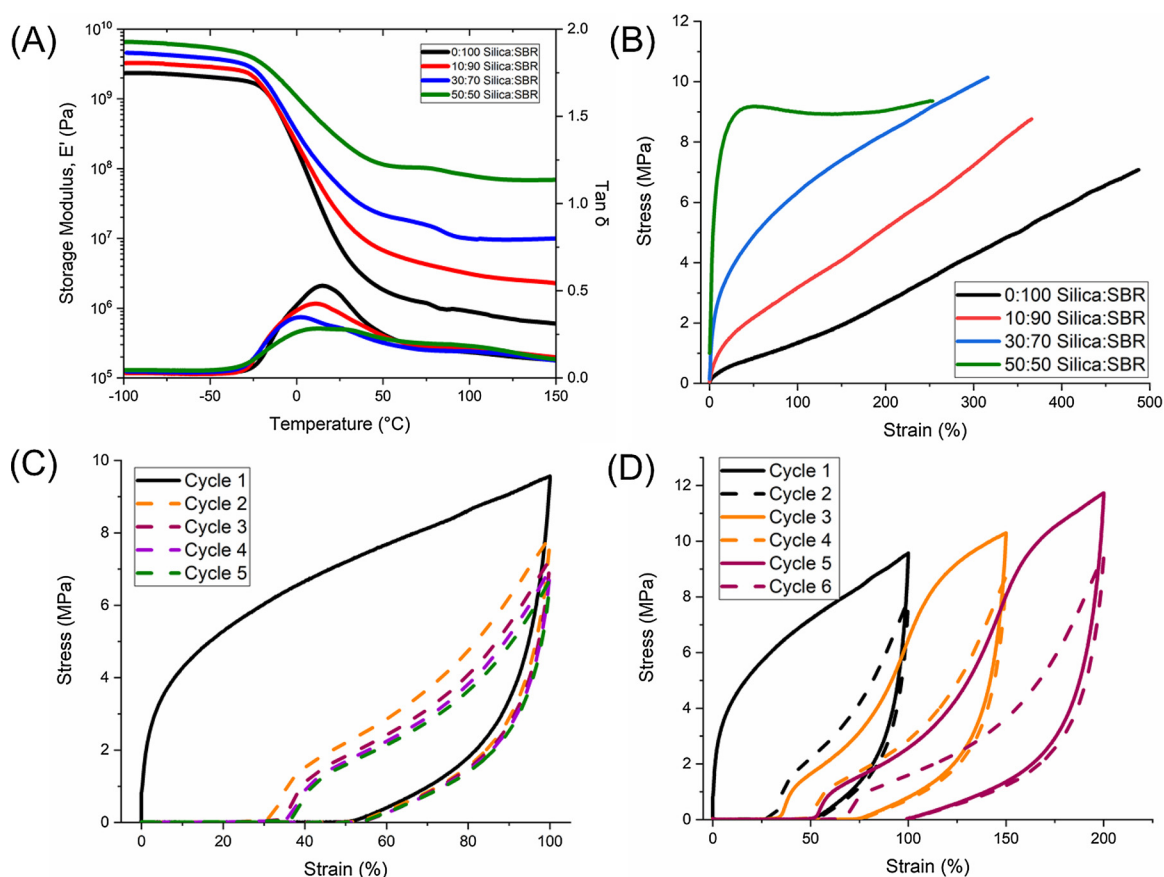


Fig. 8. (A) Dynamic mechanical analysis and (B) tensile analysis confirm silica reinforcement of sIPN nanocomposites. Cyclic tensile experiments of 30:70 Silica:SBR at a constant (C) and progressive (D) maximum strain elucidate reversible elongation and permanent set.

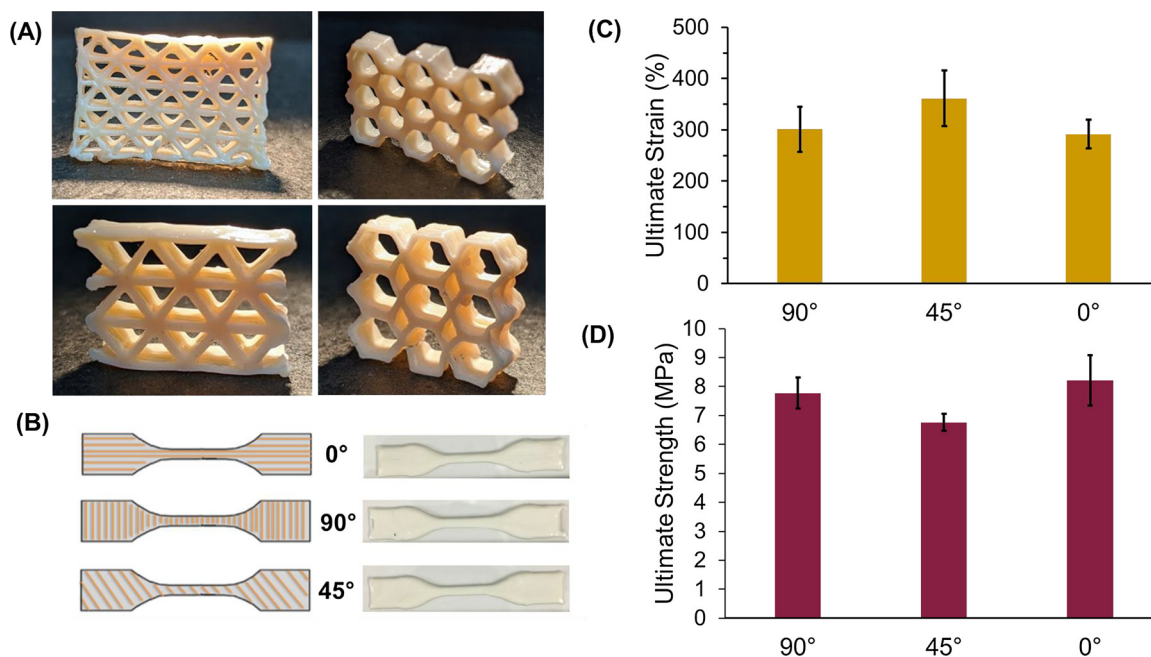


Fig. 9. (A) DIW-printed nanocomposite sIPN 3D objects from 50:50 silica:SBR photocurable hybrid colloid. (B) Graphical representation and images of UV-DIW printed dogbones (30:70 silica:SBR) with x-y layers printed at 0°, 45°, and 90° with respect to the elongation direction. (C) and (D) compare ultimate strain and stress, respectively, of the printed dogbones.

Our previous investigations of these novel sIPN's demonstrated shifting of SBR and scaffold glass transition temperatures (T_g) toward a single value due to phase-mixing [74]. The T_g 's for the nanocomposite sIPN's, as denoted by a maximum in the $\tan \delta$, remained generally consistent with the unfilled sIPN, however, these transitions became less well-defined at higher silica concentrations due to increased interactions between the silica and the sIPN network.

Tensile analysis (Fig. 8B) confirmed ultimate tensile strains above 300 % for all sIPN nanocomposites up to 30:70 silica:SBR. However, the highly filled 50:50 silica:SBR composition displayed lower ultimate tensile strains and stresses, presumably due to the much larger silica aggregates formed at this composition (see Fig. 7). Stress upon elongation also significantly increased with silica concentration. Previously, cyclic tensile experiments examined the reversible elongation of the unfilled system and attributed the occurrence of permanent set and strain softening to slippage of uncrosslinked SBR chains and breakage of the photocrosslinked scaffold [74]. Cyclic tensile experiments of 30:70 at a static (100 %, Fig. 8C) and progressively increased (100 %, 150 %, 200 %, Fig. 8D) maximum strains showed increasing plastic deformation and significant softening of the composite. Successive elongations to a constant maximum strain (Fig. 8C) illustrated significant strain softening after the first loading cycle with minimal change between subsequent cycles. Similar behavior occurred upon elongation to higher strain values (Fig. 8D), and the material exhibited lower stresses upon reloading/unloading (Cycles 2, 4, 6) than during the initial loading to each maximum strain (Cycles 1, 2, 3). This observation closely resembled the Mullins effect, which is a viscoelastic effect exaggerated by the presence and breakage of filler structures [91].

3.5. Evaluation of printed objects from UV-DIW of photocurable hybrid colloids

30:70 and 50:50 silica:SBR hybrid colloid compositions were printed via DIW due to their suitable shear yield stress behavior (Fig. 9). In agreement with predictions based on the rheological analysis, both of these compositions were extrudable at moderate pressures and, upon deposition, maintained their as-deposited shape. Moreover, these compositions maintained shape fidelity over the timescale required to print a single layer. UV irradiation subsequently photocured the paste into a robust solid green body capable of supporting subsequent layers. UV-DIW fabricated three-dimensional objects in a layer-by-layer approach, which generated elastic sIPN nanocomposite geometries upon water removal *in vacuo*.

In contrast to mask-projection VP, which fabricates entire layers simultaneously, the extrusion-based approach of DIW yields both inter-(z) and intra-(x-y) layer interfaces. These interfaces are known to create anisotropy of mechanical properties for parts fabricated by extrusion-based AM processes [49]. The extension of latex-based printing to UV-DIW affords the opportunity to study the potential of polymer particle 3D coalescence to reduce this process-induced anisotropy. The 30:70 silica:SBR composition was chosen for UV-DIW printing of tensile specimens as this ink balanced optimal rheology for printing, reinforced mechanical properties, and minimal aggregation of silica. Fig. 9C and D illustrate minimal differences between average ultimate tensile strains and stresses, respectively, for dogbones printed by UV-DIW with x-y interfaces oriented at 0°, 45°, and 90° with respect to the tensile direction (Fig. 9B). One-way ANOVA analysis determined no statistically significant difference ($p > 0.05$) for either metric across all three directions, which confirmed low anisotropy for the printed sIPN nanocomposite objects. The printed and cast 30:70 Silica:SBR samples showed similar average strains at break, 320 % and 317 %, respectively (Figs. 8 and 9). However, the printed samples showed lower average ultimate strength than the cast samples, 7.6 MPa and 8.2 MPa respectively, perhaps due to the imperfections introduced by the printing process.

4. Conclusions

Photocurable hybrid colloids present a modular and highly tunable system for additive manufacturing of elastomeric nanocomposites. Hybrid colloid design on a particle-by-particle basis (rather than as composite particles) allows for precise loading of inorganic fillers into the final nanocomposite, and the concomitant bimodal size distribution strongly directs colloidal rheology to extend latex printing to extrusion-based AM platforms. Colloidal shear-dependent liquid-solid transitions in concert with continuous-phase photocrosslinking establishes a unique processing window for UV-DIW printing that enables inks to maintain their as-deposited shape before subsequent photocuring to generate robust, stackable green body layers. Upon water removal, SBR polymer particles coalesce throughout the photocrosslinked scaffold and surround the silica nanoparticles to yield sIPN nanocomposites. These materials exhibited well-dispersed silica aggregates and significant reinforcement to (thermo)mechanical properties while retaining high ultimate strains and reversible deformation. Isotropic polymer particle coalescence throughout printed objects appeared to mitigate concerns of anisotropy due to extruded bead orientation. In sum, the design of photocurable hybrid colloids provided tunable combinations of high molecular weight elastomer and silica nanofillers. These materials exhibit suitable processability for UV-DIW and enable the fabrication of 3D architectures of high-performance elastomer nanocomposites.

Declaration of Competing Interest

This strategy for 3D printing hybrid colloids is included within the scope of a provisional patent filed by the authors (U.S. Provisional Patent Application No.: 62/823,478)

Acknowledgements

Funding for this research was provided by the Division of Civil, Mechanical, and Manufacturing Innovation (CMMI), an organization of the National Science Foundation, under award number 1762712. The authors thank our GOALI partner on this grant, Michelin North America Inc., for their collaboration and expertise throughout this work. The authors thank Steve McCartney and the Nanoscale Characterization and Fabrication Laboratory (NCFL) at Virginia Tech for expertise and instrumentation for electron microscopy. The authors also thank Prof. Michael Bortner for his rheological expertise. The authors thank Michael Berg and Nissan Chemical Corp as well as Dan Derbyshire and Mallard Creek Polymers for answering questions regarding supplied materials and their generous donation of colloidal silica nanoparticles and SBR latex, respectively.

Appendix A. Supplementary data

Supplementary material related to this article can be found, in the online version, at doi:<https://doi.org/10.1016/j.addma.2020.101393>.

References

- [1] S.K. Kumar, B.C. Benicewicz, R.A. Vaia, K.I. Winey, 50th anniversary perspective: are polymer nanocomposites practical for applications? *Macromolecules* 50 (2017) 714–731, <https://doi.org/10.1021/acs.macromol.6b02330>.
- [2] I. Momohijimoh, A.M. Hussein, N. Al-Aqeeli, Recent advances in the processing and properties of alumina-CNT/SiC nanocomposites, *Nanomater.* 9 (2019), <https://doi.org/10.3390/nano9010086>.
- [3] H. Kim, A.A. Abdala, C.W. Macosko, Graphene/polymer nanocomposites, *Macromolecules* 43 (2010) 6515–6530, <https://doi.org/10.1021/ma100572e>.
- [4] A.T. Smith, A.M. LaChance, S. Zeng, B. Liu, L. Sun, Synthesis, properties, and applications of graphene oxide/reduced graphene oxide and their nanocomposites, *Nano Mater. Sci.* 1 (2019) 31–47, <https://doi.org/10.1016/j.nanoms.2019.02.004>.
- [5] M.H. Al-Saleh, U. Sundararaj, Review of the mechanical properties of carbon nanofiber/polymer composites, *Compos. Part A Appl. Sci. Manuf.* 42 (2011)

- 2126–2142, <https://doi.org/10.1016/j.compositesa.2011.08.005>.
- [6] G. Heness, 6 - Metal-polymer nanocomposites, in: F.B.T.-A, P.N. Gao (Eds.), Woodhead Publ. Ser. Compos. Sci. Eng. Woodhead Publishing, 2012, pp. 164–177, <https://doi.org/10.1533/9780857096241.1.164>.
 - [7] R.-C. Zhang, D. Sun, R. Zhang, W.-F. Lin, M. Macias-Montero, J. Patel, S. Askari, C. McDonald, D. Mariotti, P. Maguire, Gold nanoparticle-polymer nanocomposites synthesized by room temperature atmospheric pressure plasma and their potential for fuel cell electrocatalytic application, *Sci. Rep.* 7 (2017) 46682, <https://doi.org/10.1038/srep46682>.
 - [8] C. Wang, Q. Cui, X. Wang, L. Li, Preparation of hybrid gold/polymer nanocomposites and their application in a controlled antibacterial assay, *ACS Appl. Mater. Interfaces* 8 (2016) 29101–29109, <https://doi.org/10.1021/acsami.6b12487>.
 - [9] Y. Li, X. Xu, Preparation and catalytic performance of polymer gold nanocomposites, *J. Mater. Sci.* 54 (2019) 7005–7015, <https://doi.org/10.1007/s10853-019-03342-w>.
 - [10] M. Abbas, N. Naeem (Ed.), Synthesis, Characterization and Antimicrobial Properties of Silver Nanocomposites, IntechOpen, Rijeka, 2018, <https://doi.org/10.5772/intechopen.74623> p. Ch. 4.
 - [11] J. Hoque, V. Yadav, R.G. Prakash, K. Sanyal, J. Haldar, Dual-function polymer-silver nanocomposites for rapid killing of microbes and inhibiting biofilms, *ACS Biomater. Sci. Eng.* 5 (2019) 81–91, <https://doi.org/10.1021/acsbiomaterials.8b00239>.
 - [12] N. Karak, N.B.T.-N, P.N. Karak (Eds.), Chapter 2 - Silver Nanomaterials and Their Polymer Nanocomposites, Elsevier, 2019, pp. 47–89, <https://doi.org/10.1016/B978-0-12-814615-6.00002-3>.
 - [13] L. Tamayo, M. Azócar, M. Kogan, A. Riveros, M. Páez, Copper-polymer nanocomposites: an excellent and cost-effective biocide for use on antibacterial surfaces, *Mater. Sci. Eng. C* 69 (2016) 1391–1409, <https://doi.org/10.1016/j.msec.2016.08.041>.
 - [14] M.H. Harandi, F. Alimoradi, G. Rowshan, M. Faghihi, M. Keivani, M. Abadyan, Morphological and mechanical properties of styrene butadiene rubber/nano copper nanocomposites, *Results Phys.* 7 (2017) 338–344, <https://doi.org/10.1016/j.rinp.2016.11.022>.
 - [15] M. Shahadat, T.T. Teng, M. Rafatullah, M. Arshad, Titanium-based nanocomposite materials: a review of recent advances and perspectives, *Colloids Surf. B Biointerfaces* 126 (2015) 121–137, <https://doi.org/10.1016/j.colsurf.2014.11.049>.
 - [16] A.M. Testa, S. Foglia, L. Suber, D. Fiorani, A. Roig, L. Casas, E. Molins, J. M. J. Tejada, G.C. Hadjipanyis (Ed.), Magnetic Properties of Iron Oxide Nanocomposites BT - Magnetic Storage Systems Beyond 2000, Springer Netherlands, Dordrecht, 2001, pp. 411–419, https://doi.org/10.1007/978-94-010-0624-8_37.
 - [17] N.H. Abdullah, K. Shamel, E.C. Abdullah, L.C. Abdullah, Solid matrices for fabrication of magnetic iron oxide nanocomposites: synthesis, properties, and application for the adsorption of heavy metal ions and dyes, *Compos. Part B Eng.* 162 (2019) 538–568, <https://doi.org/10.1016/j.compositesb.2018.12.075>.
 - [18] E. Diaz, P. Brousseau, G. Ampleman, R.E. Prud'homme, Polymer nanocomposites from energetic thermoplastic elastomers and Alex®, propellants, *Explos. Pyrotech.* 28 (2003) 210–215, <https://doi.org/10.1002/prep.200300007>.
 - [19] M.M. Khani, Z.M. Abbas, B.C. Benicewicz, Well-defined polyisoprene-grafted silica nanoparticles via the RAFT process, *J. Polym. Sci. Part A: Polym. Chem.* 55 (2017) 1493–1501, <https://doi.org/10.1002/pola.28514>.
 - [20] M.M. Khani, D. Woo, E.L. Mumpower, B.C. Benicewicz, Poly(alkyl methacrylate)-grafted silica nanoparticles in polyethylene nanocomposites, *Polymer (Guildf.)* 109 (2017) 339–348, <https://doi.org/10.1016/j.polymer.2016.12.046>.
 - [21] S.K. Kumar, N. Jouault, B. Benicewicz, T. Neely, Nanocomposites with polymer grafted nanoparticles, *Macromolecules* 46 (2013) 3199–3214, <https://doi.org/10.1021/ma4001385>.
 - [22] D. Carolan, A. Ivankovic, A.J. Kinloch, S. Sprenger, A.C. Taylor, Toughening of epoxy-based hybrid nanocomposites, *Polymer (Guildf.)* 97 (2016) 179–190, <https://doi.org/10.1002/j.polymer.2016.05.007>.
 - [23] W. Li, Z. Qiu, M. Tebyetekerwa, J. Zhang, Y. Wang, T. Gao, J. Wang, Y. Ding, Y. Xie, Preparation of silica/polymer nanocomposites with aggregation-induced emission properties as fluorescent responsive coatings, *Prog. Org. Coatings* 127 (2019) 8–15, <https://doi.org/10.1016/j.porgcoat.2018.11.001>.
 - [24] A. Kongsinlark, G. Rempel, P. Prasassarakich, Hydrogenated polyisoprene-silica nanoparticles and their applications for nanocomposites with enhanced mechanical properties and thermal stability, *J. Nanopart. Res.* 15 (2013) 1–16, <https://doi.org/10.1007/s11051-013-1612-7>.
 - [25] G. Malucelli, R. Bongiovanni, M. Sangermano, S. Ronchetti, A. Priola, Preparation and characterization of UV-cured epoxy nanocomposites based on o-montmorillonite modified with maleinized liquid polybutadienes, *Polymer (Guildf.)* 48 (2007) 7000–7007, <https://doi.org/10.1016/j.polymer.2007.10.008>.
 - [26] Y. Chen, A.M. Kushner, G.A. Williams, Z. Guan, Multiphase design of autonomic self-healing thermoplastic elastomers, *Nat. Chem.* 4 (2012) 467–472, <https://doi.org/10.1038/nchem.1314>.
 - [27] D.D.J. Rousseaux, N. Sallem-Idrissi, A.-C. Baudouin, J. Devaux, P. Godard, J. Marchand-Brynaert, M. Sclavons, Water-assisted extrusion of polypropylene/clay nanocomposites: a comprehensive study, *Polymer (Guildf.)* 52 (2011) 443–451, <https://doi.org/10.1016/j.polymer.2010.11.027>.
 - [28] H. Zhao, R.K.Y. Li, A study on the photo-degradation of zinc oxide (ZnO) filled polypropylene nanocomposites, *Polymer (Guildf.)* 47 (2006) 3207–3217, <https://doi.org/10.1016/j.polymer.2006.02.089>.
 - [29] K. Xu, S. Zhou, L. Wu, Dispersion of γ -methacryloxypropyltrimethoxysilane-functionalized zirconia nanoparticles in UV-curable formulations and properties of their cured coatings, *Prog. Org. Coatings* 67 (2010) 302–310, <https://doi.org/10.1016/j.porgcoat.2009.10.029>.
 - [30] I. Yamaguchi, K. Tokuchi, H. Fukuzaki, Y. Koyama, K. Takakuda, H. Monma, J. Tanaka, Preparation and microstructure analysis of chitosan/hydroxyapatite nanocomposites, *J. Biomed. Mater. Res.* 55 (2001) 20–27, [https://doi.org/10.1002/1097-4636\(200104\)55:1<20::AID-JBM30>3.0.CO;2-F](https://doi.org/10.1002/1097-4636(200104)55:1<20::AID-JBM30>3.0.CO;2-F).
 - [31] M. Aguirre, M. Paulis, J.R. Leiza, UV screening clear coats based on encapsulated CeO₂ 2 hybrid latexes, (n.d.), 10.1039/c2ta00762b.
 - [32] N. Zgheib, J.-L. Putaux, A. Thill, E. Bourgeat-Lami, F. D'Agosto, M. Lansalot, Cerium oxide encapsulation by emulsion polymerization using hydrophilic macroRAFT agents, *Polym. Chem.* 4 (2013) 607–614, <https://doi.org/10.1039/C2PY20548C>.
 - [33] N.B. Palaganas, J.D. Mangadiao, A.C.C. de Leon, J.O. Palaganas, K.D. Pangilinan, Y.J. Lee, R.C. Advincula, 3D printing of photocurable cellulose nanocrystal composite for fabrication of complex architectures via stereolithography, *ACS Appl. Mater. Interfaces* 9 (2017) 34314–34324, <https://doi.org/10.1021/acsami.7b09223>.
 - [34] M. Fardoui, Ael K. Qaiss, R. Bouhfid, 16 - cellulose nanocrystal-based nanocomposites, in: M. Jawaid, S. Boufi, A.K.B.T.-C.-R.N.C. H.P.S. (Eds.), Woodhead Publ. Ser. Compos. Sci. Eng. Woodhead Publishing, 2017, pp. 373–389, <https://doi.org/10.1016/B978-0-08-100957-4.00016-4>.
 - [35] N.-A. Rangel-Vazquez, S. Thomas, J. Datta, J.T. Haponiuk, A.B.T.-P.P. Reghunadhan (Eds.), Chapter 10 - Nanocomposites of PU Polymers With Nano Chitin and Nano Starch, Elsevier, Amsterdam, 2017, pp. 311–336, <https://doi.org/10.1016/B978-0-12-804065-2.00010-3>.
 - [36] H. Sehaqui, K. Kulasinski, N. Pfenninger, T. Zimmermann, P. Tingaut, Highly carboxylated cellulose nanofibers via succinic anhydride esterification of wheat fibers and facile mechanical disintegration, *Biomacromolecules* 18 (2017) 242–248, <https://doi.org/10.1021/acs.biomac.6b01548>.
 - [37] E. Jamroz, P. Kulawik, P. Kopel, The effect of nanofillers on the functional properties of biopolymer-based films: a review, *Polymers (Basel)* 11 (2019) 675, <https://doi.org/10.3390/polym11040675>.
 - [38] K.-U. Jeong, J.Y. Lim, J.-Y. Lee, S.L. Kang, C. Nah, Polymer nanocomposites reinforced with multi-walled carbon nanotubes for semiconducting layers of high-voltage power cables, *Polym. Int.* 59 (2010) 100–106, <https://doi.org/10.1002/pi.2696>.
 - [39] R. Zhang, K. Moon, W. Lin, C.P. Wong, Preparation of highly conductive polymer nanocomposites by low temperature sintering of silver nanoparticles, *J. Mater. Chem.* 20 (2010) 2018–2023, <https://doi.org/10.1039/B921072E>.
 - [40] Prateek, V.K. Thakur, R.K. Gupta, Recent progress on ferroelectric polymer-based nanocomposites for high energy density capacitors: synthesis, dielectric properties, and future aspects, *Chem. Rev.* 116 (2016) 4260–4317, <https://doi.org/10.1021/acs.chemrev.5b00495>.
 - [41] L.L. Beecroft, C.K. Ober, Nanocomposite materials for optical applications, *Chem. Mater.* 9 (1997) 1302–1317, <https://doi.org/10.1021/cm960441a>.
 - [42] R.A. Hule, D.J. Pochan, Polymer nanocomposites for biomedical applications, *MRS Bull.* 32 (2007) 354–358, <https://doi.org/10.1557/mrs2007.235>.
 - [43] W. Kaewsakul, K. Sahakaro, W.K. Dierkes, J.W.M. Noordermeer, Optimization of mixing conditions for silica-reinforced natural rubber tire tread compounds, *Rubber Chem. Technol.* 85 (2012) 277–294.
 - [44] L. Xia, J. Song, H. Wang, Z. Kan, Silica nanoparticles reinforced natural rubber latex composites: the effects of silica dimension and polydispersity on performance, *J. Appl. Polym. Sci.* 136 (2019) 47449, <https://doi.org/10.1002/app.47449>.
 - [45] B.B. Boonstra, H. Cochrane, E.M. Dannenberg, Reinforcement of silicone rubber by particulate silica, *Rubber Chem. Technol.* 48 (1975) 558–576.
 - [46] E. Bourgeat-Lami, M. Lansalot, A.M. van Herk, K. Landfester (Eds.), Organic/Inorganic Composite Latexes: The Marriage of Emulsion Polymerization and Inorganic Chemistry BT - Hybrid Latex Particles: Preparation With (Mini)Emulsion Polymerization, Springer, Berlin Heidelberg, Berlin, Heidelberg, 2010, pp. 53–123, https://doi.org/10.1007/12_2010_60.
 - [47] S. Varghese, K.G. Gatos, A.A. Apostolov, J. Karger-Kocsis, Morphology and mechanical properties of layered silicate reinforced natural and polyurethane rubber blends produced by latex compounding, *J. Appl. Polym. Sci.* 92 (2004) 543–551, <https://doi.org/10.1002/app.20036>.
 - [48] J. Tao, D. He, B. Tang, L. Kong, Y. Luo, P. Zhao, W. Gong, Z. Peng, In situ synthesis of natural rubber latex-supported gold nanoparticles for flexible SERS substrates, *RSC Adv.* 5 (2015) 49168–49174, <https://doi.org/10.1039/C5RA05681K>.
 - [49] I. Gibson, D.W. Rosen, B. Stucker, Additive Manufacturing Technologies, Springer Science + Business Media, LLC, New York, NY, 2010, <https://doi.org/10.1007/978-1-4419-1120-9>.
 - [50] K. Chen, X. Kuang, Y. Li, G. Kang, H.J. Qi, Fabrication of tough epoxy with shape memory effects by UV-assisted direct-ink write printing, *Soft Matter* 14 (2018) 1879–1886, <https://doi.org/10.1039/C7SM02362F>.
 - [51] A. M'Barki, L. Bocquet, A. Stevenson, Linking rheology and printability for dense and strong ceramics by direct ink writing, *Sci. Rep.* 7 (2017) 6017, <https://doi.org/10.1038/s41598-017-06115-0>.
 - [52] O. Rios, W. Carter, B. Post, P. Lloyd, D. Fenn, C. Kutchko, R. Rock, K. Olson, B. Compton, 3D printing via ambient reactive extrusion, *Mater. Today Commun.* 15 (2018) 333–336, <https://doi.org/10.1016/j.mtcomm.2018.02.031>.
 - [53] A. Corker, H.C.-H. Ng, R.J. Poole, E. García-Tuñón, 3D printing with 2D colloids: designing rheology protocols to predict 'printability' of soft-materials, *Soft Matter* 15 (2019) 1444–1456, <https://doi.org/10.1039/C8SM01936C>.
 - [54] B.G. Compton, J.A. Lewis, 3D-printing of lightweight cellular composites, *Adv. Mater.* 26 (2014) 5930–5935, <https://doi.org/10.1002/adma.201401804>.
 - [55] D.A. Rau, J. Herzberger, T.E. Long, C.B. Williams, Ultraviolet-assisted direct ink write to additively manufacture all-aromatic polyimides, *ACS Appl. Mater. Interfaces* 10 (2018) 34828–34833, <https://doi.org/10.1021/acsami.8b14584>.
 - [56] C. Zhu, A.J. Pascall, N. Dudukovic, M.A. Worsley, J.D. Kuntz, E.B. Duoss,

- C.M. Spadaccini, Colloidal materials for 3D printing, *Annu. Rev. Chem. Biomol. Eng.* 10 (2019) 17–42, <https://doi.org/10.1146/annurev-chembioeng-060718-030133>.
- [57] J.E. Smay, J. Cesarano, J.A. Lewis, Colloidal inks for directed assembly of 3-D periodic structures, *Langmuir* 18 (2002) 5429–5437, <https://doi.org/10.1021/la0257135>.
- [58] G.M. Gratson, J.A. Lewis, Phase behavior and rheological properties of polyelectrolyte inks for direct-write assembly, *Langmuir* 21 (2005) 457–464, <https://doi.org/10.1021/la048228d>.
- [59] I.D. Robertson, M. Yourdkhani, P.J. Centellas, J.E. Aw, D.G. Ivanoff, E. Goli, E.M. Lloyd, L.M. Dean, N.R. Sottos, P.H. Geubelle, J.S. Moore, S.R. White, Rapid energy-efficient manufacturing of polymers and composites via frontal polymerization, *Nature* 557 (2018) 223–227, <https://doi.org/10.1038/s41586-018-0054-x>.
- [60] Q. Shi, K. Yu, X. Kuang, X. Mu, C.K. Dunn, M.L. Dunn, T. Wang, H. Jerry Qi, Recyclable 3D printing of vitrimer epoxy, *Mater. Horizons* 4 (2017) 598–607, <https://doi.org/10.1039/C7MH00043J>.
- [61] S.-Z. Guo, F. Gosselin, N. Guerin, A.-M. Lanouette, M.-C. Heuzey, D. Theriault, Solvent-cast three-dimensional printing of multifunctional microsystems, *Small* 9 (2013) 4118–4122, <https://doi.org/10.1002/sml.201300975>.
- [62] A. Hamidi, Y. Tadesse, 3D printing of very soft elastomer and sacrificial carbohydrate glass/elastomer structures for robotic applications, *Mater. Des.* 187 (2020) 108324, <https://doi.org/10.1016/j.matdes.2019.108324>.
- [63] G. Siqueira, D. Kokkinis, R. Libanori, M.K. Hausmann, A.S. Gladman, A. Neels, P. Tingaut, T. Zimmermann, J.A. Lewis, A.R. Studart, Cellulose nanocrystal inks for 3D printing of textured cellular architectures, *Adv. Funct. Mater.* 27 (2017) 1604619, <https://doi.org/10.1002/adfm.201604619>.
- [64] A.P. Haring, E.G. Thompson, Y. Tong, S. Laheri, E. Cesewski, H. Sontheimer, B.N. Johnson, Process- and bio-inspired hydrogels for 3D bioprinting of soft free-standing neural and glial tissues, *Biofabrication* 11 (2019) 25009, <https://doi.org/10.1088/1758-5090/ab02c9>.
- [65] J.E. Smay, G.M. Gratson, R.F. Shepherd, J. Cesarano III, J.A. Lewis, Directed colloidal assembly of 3D periodic structures, *Adv. Mater.* 14 (2002) 1279–1283, [https://doi.org/10.1002/1521-4095\(20020916\)14:18<1279::AID-ADMA1279>3.0.CO;2-A](https://doi.org/10.1002/1521-4095(20020916)14:18<1279::AID-ADMA1279>3.0.CO;2-A).
- [66] T. Wu, P. Jiang, X. Zhang, Y. Guo, Z. Ji, X. Jia, X. Wang, F. Zhou, W. Liu, Additively manufacturing high-performance bismaleimide architectures with ultraviolet-assisted direct ink writing, *Mater. Des.* 180 (2019) 107947, <https://doi.org/10.1016/j.matdes.2019.107947>.
- [67] R.A. Barry III, R.F. Shepherd, J.N. Hanson, R.G. Nuzzo, P. Wiltzius, J.A. Lewis, Direct-write assembly of 3D hydrogel scaffolds for guided cell growth, *Adv. Mater.* 21 (2009) 2407–2410, <https://doi.org/10.1002/adma.200803702>.
- [68] E.N. Udofia, W. Zhou, A guiding framework for microextrusion additive manufacturing, *J. Manuf. Sci. Eng.* 141 (2019), <https://doi.org/10.1115/1.4042607>.
- [69] J.J. Fallon, S.H. McKnight, M.J. Bortner, Highly loaded fiber filled polymers for material extrusion: a review of current understanding, *Addit. Manuf.* 30 (2019) 100810, <https://doi.org/10.1016/j.addma.2019.100810>.
- [70] N. Willenbacher, K. Georgieva, Rheology of disperse systems, *Prod. Des. Eng.* (2013) 7–49.
- [71] J.S. Chong, E.B. Christiansen, A.D. Baer, Rheology of concentrated suspensions, *J. Appl. Polym. Sci.* 15 (1971) 2007–2021, <https://doi.org/10.1002/app.1971.070150818>.
- [72] Z. Jiang, O. Erol, D. Chatterjee, W. Xu, N. Hibino, L.H. Romer, S.H. Kang, D.H. Gracias, Direct ink writing of poly(tetrafluoroethylene) (PTFE) with tunable mechanical properties, *ACS Appl. Mater. Interfaces* 11 (2019) 28289–28295, <https://doi.org/10.1021/acsami.9b07279>.
- [73] S. Roh, D.P. Parekh, B. Bharti, S.D. Stoyanov, O.D. Velev, 3D printing by multiphase silicone/water capillary inks, *Adv. Mater.* 29 (2017), <https://doi.org/10.1002/adma.201701554> 1701554-n/a.
- [74] P.J. Scott, V. Meenakshisundaram, M. Hegde, C. Kasprzak, C. Winkler, K. Feller, C.B. Williams, T.E. Long, 3D printing latex: a route to complex geometries of high molecular weight polymers, *ACS Appl. Mater. Interfaces* 12 (2020) 10918–10928, <https://doi.org/10.1021/acsami.9b19986>.
- [75] B.D. Fairbanks, M.P. Schwartz, C.N. Bowman, K.S. Anseth, Photoinitiated polymerization of PEG-diacrylate with lithium phenyl-2,4,6-trimethylbenzoylphosphinate: polymerization rate and cytocompatibility, *Biomaterials* 30 (2009) 6702–6707, <https://doi.org/10.1016/j.biomaterials.2009.08.055>.
- [76] T. Majima, W. Schnabel, W. Weber, Phenyl-2,4,6-trimethylbenzoylphosphinates as water-soluble photoinitiators. Generation and reactivity of $O=P(C_6H_5)(O^-)$ radical anions, *Die Makromol. Chem.* 192 (1991) 2307–2315, <https://doi.org/10.1002/macp.1991.021921010>.
- [77] B.M. Cash, L. Wang, B.C. Benicewicz, The preparation and characterization of carboxylic acid-coated silica nanoparticles, *J. Polym. Sci. Part A: Polym. Chem.* 50 (2012) 2533–2540, <https://doi.org/10.1002/pola.26029>.
- [78] K. Takamura, T.G.M. van de Ven, Shear thinning behavior of concentrated latex dispersions, *Macromol. Symp.* 288 (2010) 78–86, <https://doi.org/10.1002/masy.201050210>.
- [79] G. Wypych, *Handbook of Polymers*, 2nd ed., ChemTec Publishing, Toronto, 2016.
- [80] S. Ji, J.Y. Walz, Interaction potentials between two colloidal particles surrounded by an extremely bidisperse particle suspension, *J. Colloid Interface Sci.* 394 (2013) 611–618, <https://doi.org/10.1016/j.jcis.2012.11.040>.
- [81] J.L. Harden, H. Guo, M. Bertrand, T.N. Shendruk, S. Ramakrishnan, R.L. Leheny, Enhanced gel formation in binary mixtures of nanocolloids with short-range attraction, *J. Chem. Phys.* 148 (2018) 44902, <https://doi.org/10.1063/1.5007038>.
- [82] S. Asakura, F. Oosawa, On interaction between two bodies immersed in a solution of macromolecules, *J. Chem. Phys.* 22 (1954) 1255–1256, <https://doi.org/10.1063/1.1740347>.
- [83] S. Asakura, F. Oosawa, Interaction between particles suspended in solutions of macromolecules, *J. Polym. Sci.* 33 (1958) 183–192, <https://doi.org/10.1002/pol.1958.1203312618>.
- [84] P.J. Lu, E. Zaccarelli, F. Ciulla, A.B. Schofield, F. Sciortino, D.A. Weitz, Gelation of particles with short-range attraction, *Nature* 453 (2008) 499–503, <https://doi.org/10.1038/nature06931>.
- [85] M. Dijkstra, D. Frenkel, J. Hansen, Phase separation in binary hard-core mixtures, *J. Chem. Phys.* 101 (1994) 3179–3189, <https://doi.org/10.1063/1.468468>.
- [86] S. Buzzaccaro, R. Rusconi, R. Piazza, “Sticky” hard spheres: equation of state, phase diagram, and metastable gels, *Phys. Rev. Lett.* 99 (2007) 98301, <https://doi.org/10.1103/PhysRevLett.99.098301>.
- [87] A. Yu Zubarev, L.Y. Isakova, Condensation phase transitions in bidisperse colloids, *Phys. A Stat. Mech. Its Appl.* 349 (2005) 1–10, <https://doi.org/10.1016/j.physa.2004.09.024>.
- [88] Y. Mao, M.E. Cates, H.N.W. Lekkerkerker, Depletion force in colloidal systems, *Phys. A Stat. Mech. Its Appl.* 222 (1995) 10–24, [https://doi.org/10.1016/0378-4371\(95\)00206-5](https://doi.org/10.1016/0378-4371(95)00206-5).
- [89] J.W. Halloran, Ceramic stereolithography: additive manufacturing for ceramics by photopolymerization, *Annu. Rev. Mater. Res.* 46 (2016) 19–40, <https://doi.org/10.1146/annurev-matsci-070115-031841>.
- [90] M. Hegde, V. Meenakshisundaram, N. Chartrain, S. Sekhar, D. Tafti, C.B. Williams, T.E. Long, 3D printing all-aromatic polyimides using mask-projection stereolithography: processing the nonprocessable, *Adv. Mater.* 29 (2017) 1701240, <https://doi.org/10.1002/adma.201701240>.
- [91] A. Dorfmann, R.W. Ogden, A constitutive model for the Mullins effect with permanent set in particle-reinforced rubber, *Int. J. Solids Struct.* 41 (2004) 1855–1878, <https://doi.org/10.1016/j.ijsolstr.2003.11.014>.